JOURNAL OF MATERIALS SCIENCE 21 (1986) 1491–1501

# Fracture toughness anisotropy of a pyrolytic carbon

M. SAKAI*, R. C. BRADT, D. B. FISCHBACH
*Department of Materials Science and Engineering, FB-10, College of Engineering, University of Washington, Seattle, Washington 98195, USA*

The anisotropic flexural strengths, static Young's moduli and the corresponding fracture toughnesses were measured for the three orthogonal fracture surface orientations, $S_{ca}$ (interlaminar cleavage), $S_{bc}$ and $S_{ab}$ (layer rupture across and along the layers, respectively), of an as deposited substrate-nucleated pyrolytic carbon. Both $S_{ca}$ delamination and $S_{ab}$ along-layer rupture produced smooth fracture surfaces with mean $K_{Ic}$ values (MPa m$^{1/2}$) of 0.53 for $S_{ca}$ and 0.93 for $S_{ab}$, independent of notch length. A different type of behaviour was observed for $S_{bc}$ across-layer fracture. Delamination cracking during failure resulted in rough fracture surfaces, crack arrests, and high apparent toughness values dependent on sample size and crack length. The nature of this induced delamination toughening is discussed.

## 1. Introduction

The mechanical properties of the common forms of polygranular synthetic carbons and graphites often exhibit marked non-linearities due to the combined effects of the strong intrinsic anisotropy of the graphite layer structure, and extensive inelastic microcracking and slippage at the crystalline interfaces and filler/matrix boundaries. Although these non-linearities may cause considerable difficulty during fracture mechanics studies of these materials, several such investigations have been reported over the last decade [1–4]. Recently, Sakai *et al.* [5] have developed a quantitative experimental method to separate the elastic and inelastic contributions to the crack extension energy. They concluded that 30 to 40% of the total energy dissipation during crack extension in synthetic graphites can be consumed by inelastic processes.

A complete understanding of the non-linear inelastic fracture mechanisms in graphitic materials is difficult because of their microstructural complexity and its role in microcracking and slippage processes. Studies of materials with simpler, well-defined microstructures are needed to facilitate a more fundamental understanding of the complex fracture processes in carbons and graphites. The near ideal density and the laminar microstructure of pyrolytic carbon recommend it for such a study, one directed toward understanding of the intrinsic fracture behaviour of carbon and graphite materials. Investigation of a substrate-nucleated pyrolytic carbon by fracture mechanics and energy methods is the main objective of the present work. Values of the anisotropic fracture toughnesses and the appreciable toughening that can result from induced delamination cracking are reported and discussed.

## 2. Pyrolytic carbons

The production and properties of pyrolytic carbon have been reviewed in detail by Smith and Leeds [6]. Pyrolytic carbons are formed by chemical vapour deposition from hydrocarbon gases on substrates that are, typically, polygranular synthetic graphites. Deposits made in hot-wall furnaces at elevated temperatures (1900 to 2300° C) and low source gas concentrations yield substantially homogeneous, dense ($\sim 2.2\,\mathrm{g\,cm^{-3}}$), anisotropic, brittle carbons with a strong sheet-type layer orientation texture. Deposition nucleates primarily at irregularities on the substrate surface, resulting in a characteristic columnar "growth cone" structure comprising graphitic hexagonal layers with apparent (diffraction coherence-length) diameters of 10 to 30 nm that are aligned approximately parallel to the substrate, with random stacking and a mean interlayer spacing, $d_{002} \simeq 0.344\,\mathrm{nm}$ (turbostratic carbon). For physical property considerations, the structural morphology of pyrolytic carbon may be conveniently approximated by a simple model comprising a wrinkled stack of parallel sheets. Although this type of pyrolytic carbon is sometimes called pyrolytic graphite, that terminology is appropriate only for material that has been heat treated at temperatures > 2700° C to develop the regular ABAB layer stacking sequence of hexagonal crystalline graphite.

Some aspects of the anisotropic nature of the mechanical failure of substrate-nucleated pyrolytic carbon were investigated by Berry and Gebhardt [7] using optical microscopy. They have reported that in addition to interlaminar cleavage, two distinct types of layer rupture fracture surfaces, corresponding to crack propagation parallel to or perpendicular to the layers, may be obtained. The appearances of these two

---

*On leave from Toyohashi University of Technology, Tempaku-cho, Toyohashi 440, Japan.

0022–2461/86 $03.00 + .12

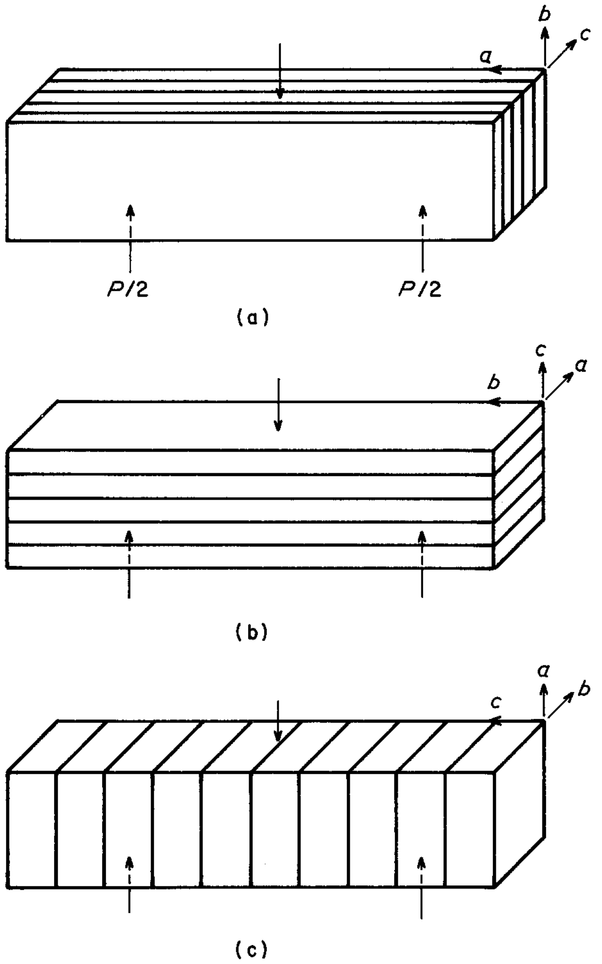

*Figure 1* The three flexural deformation orientations $D_{ij}$ of pyrolytic carbon. (a) $D_{ab}$; (b) $D_{bc}$; (c) $D_{ca}$.

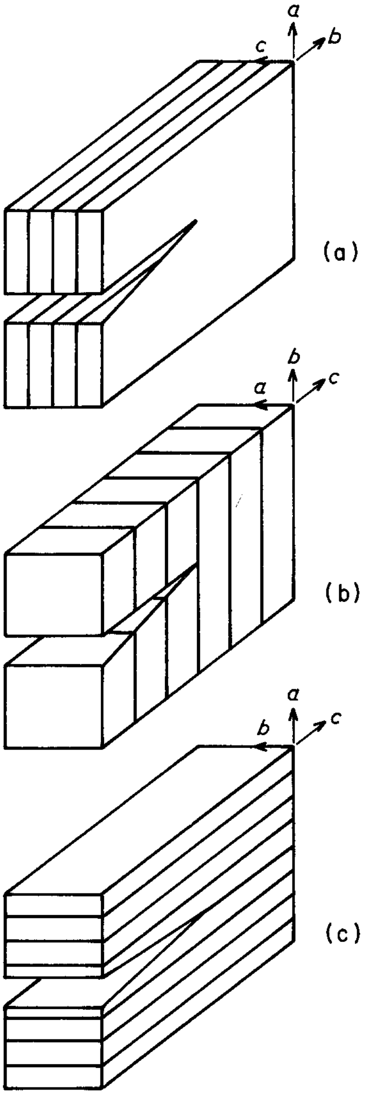

*Figure 2* The three fracture surface orientations $S_{ij}$ of pyrolytic carbon, illustrated for a compact-tension specimen geometry. (a) $S_{ab}$; (b) $S_{bc}$; (c) $S_{ca}$.

latter fracture surfaces are quite different. The surface for the parallel crack extension is smooth and gently undulating, but that for the perpendicular propagation direction is rough and irregular with a distinct parallel-to-layer texture. These characteristics of the fracture surfaces were later confirmed in more detail by scanning electron microscopy [8] and imply significant differences in the effective fracture surface energies for the different crack orientations.

## 3. Deformation and fracture modes of pyrolytic carbon

In laminar materials such as pyrolytic carbon there are three distinct flexural deformations, $D_{ij}$, and three corresponding crack opening fracture surface orientations, $S_{ij}$, where $i, j = a, b$, or $c$ are the principal axes of the material. In pyrolytic carbon, $c$ is perpendicular to the deposition plane (the average layer plane orientation) while $a$ and $b$ are equivalent orthogonal axes within the deposition plane, parallel to the layers.

In the deformation designation, $D_{ij}$, the initial subscript, $i$, indicates the direction of the tensile (or compressive) stress during bending, while $j$ is the direction of the deflection (perpendicular to the stress and parallel to the applied load). The three deformations $D_{ab}$, $D_{bc}$ and $D_{ca}$ are illustrated in Fig. 1. For example, $D_{ab}$ represents deformation with both the tensile stress ($a$-direction) and the deflection ($b$-direction) parallel to the layers. The other two deformations are similarly defined. $D_{bc}$ is termed "the parallel orientation" and $D_{ab}$ "the perpendicular orientation" by Berry and Gebhardt [7].

The three corresponding opening-mode fracture surface orientations are $S_{ab}$, $S_{bc}$, and $S_{ca}$. These are illustrated in Fig. 2 for a fracture specimen geometry. In the notation $S_{ij}$, $i$ denotes the direction normal to the surface and $j$ the direction of crack propagation. For example, $S_{bc}$ means that the fracture surface is nominally perpendicular to the layers (normal to the $b$-axis) and the crack propagates perpendicular to the layers ($c$-direction). Generally, the $D_{ab}$ deformation may be expected to yield an $S_{ab}$ fracture surface, $D_{bc}$ an $S_{bc}$, and $D_{ca}$ an $S_{ca}$ surface.

## 4. Experimental procedure

A commercial* substrate-nucleated pyrolytic carbon in the form of an 11 mm thick plate deposited from natural gas at about 2200° C was obtained for study.

*Super Temp. Co., 11120 S Norwalk Boulevard, Santa Fe Springs, California 90670, USA.

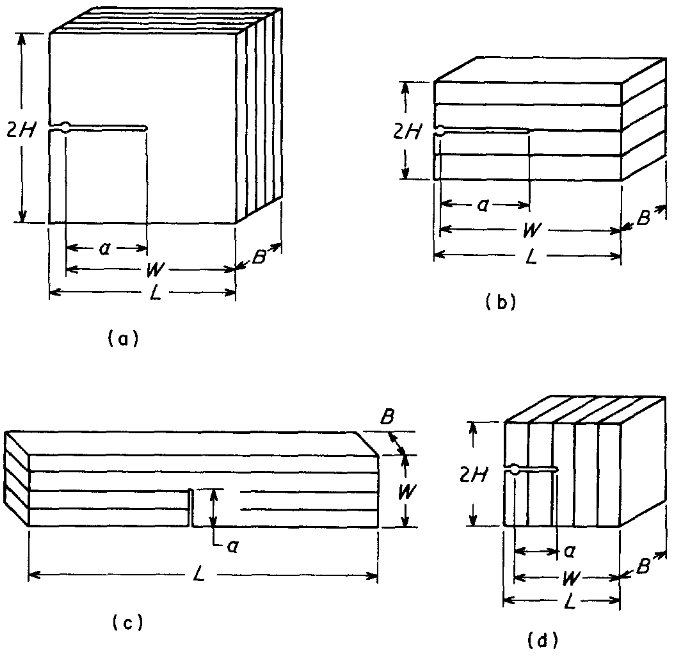

*Figure 3* Geometries and dimensions of the fracture mechanics specimens. (a) $S_{ab}$ (CT); (b) $S_{ca}$ (DCB); (c) $S_{bc}$ (three-point bend); (d) $S_{bc}$ (CT).

| | | $B$(mm) | $2H$(mm) | $L$(mm) | $W$(mm) |
|---|---|---|---|---|---|
| $S_{ab}$ | (CT) | 11.0 | 24.8 | 24.8 | 20.4 |
| $S_{bc}$ | (Three-point bend) | 9.5 | SPAN 38.1 | 50.5 | 11.0 |
| | (CT) | 10.5 | 15.5 | 11.0 | 10.0 |
| $S_{ca}$ | (DCB) | 10.0 | 11.0 | 24.8 | 22.0 |

Its bulk density is 2.186 g cm$^{-3}$. The mean interlayer spacing, as determined from the (0 0 4) X-ray diffraction line, is $d_{002} = 0.344$ nm. From these results it may be inferred that the micropore volume is about 1%[†]. The layer orientation distribution function $I(\omega)/I(0)$ was determined by measuring the intensity $I(\omega)$ of the (0 0 2) X-ray diffraction peak as a function of the angle $\omega$ between the diffraction vector and the normal to the deposition plane using a thin bar sample ($1 \times 1.5 \times 10$ mm$^3$) cut from the plane of the deposit. The half-width at half-maximum intensity was 20° and the distribution fit Bacon's expression, $I(\omega)/I(0) = \cos^n\omega$ with $n = 11$, yielding a root-mean-square misorientation angle of 17.5° [9].

Fracture testing employed standard fracture mechanics geometries in the opening mode (Mode I) for each of the three crack-plane orientations. These specimens are shown in Fig. 3. Double cantilever beam (DCB) specimens were used for the $S_{ca}$ orientation and compact tension (CT) specimens for $S_{ab}$. Both CT and notched three-point bend specimens were used for the $S_{bc}$ orientation. In practice, the $S_{bc}$-oriented CT specimens always failed by delamination ($S_{ca}$ type fracture) for all notch depths. Therefore, it was necessary to use the three-point bend specimens (38.1 mm span) to obtain $S_{bc}$ fracture. Fracture data were obtained as a function of notch depth in the $(a/W) = \alpha$ range of 0.2 to 0.8. Notches were cut with a 0.6 mm thick diamond saw and then extended about 0.5 mm with a very thin saw made from a razor blade to finally yield a sharp crack. The resulting tip radius, $\simeq 10\,\mu$m, was suitable for reliable $K_{\mathrm{Ic}}$ measurement [10].

Load ($P$) against loadpoint displacement ($u$) curves for the CT and DCB specimens were determined with a commercial testing machine (Instron Model 1122). The test arrangement is shown schematically in Fig. 4. The load was applied via steel wire loops confined in grooves near the beginning of the notch, formed by drilling a hole before the notch was sawed. The load was measured with a load cell. The loadpoint displacement was measured with a strain-gauge extensometer (Instron G-51-11) bearing on two small aluminium blocks glued to the end of the specimen. The displacement ($u$) at the load point was computed from the measured displacement $u$(exp) at the face of the aluminium blocks using the proportionality relationship $u/u(\text{exp}) = a/(L + t - W + a)$, where $t$ is the block thickness and $L$, $W$ and $a$ are specimen dimensions; and rigid-beam deflection about the notch tip is assumed. The load was applied incrementally to facilitate accurate determination of the ($P$–$u$) curves from separately recorded load and displacement data.

For the bend specimens, load against time curves were recorded at a constant crosshead speed (0.05 mm min$^{-1}$) and the specimen deflection was calculated from the crosshead displacement, corrected for the machine compliance which was small. Un-notched three-point flexure (Modulus of Rupture) specimens for all three deformation orientations were also tested

---

[†] For crystalline graphite $d_{002} = 0.3354$ nm and the ideal density is 2.266 g cm$^{-3}$. The turbostratic disorder in PC increases $d_{002}$ but has negligible effect on the in-plane atomic spacing; thus the ideal density of this pyrolytic carbon is $2.266\,(0.3354/0.344) = 2.209$ g cm$^{-3}$. The volume fraction of pores is then $1 - (2.186/2.209) \simeq 0.01$.

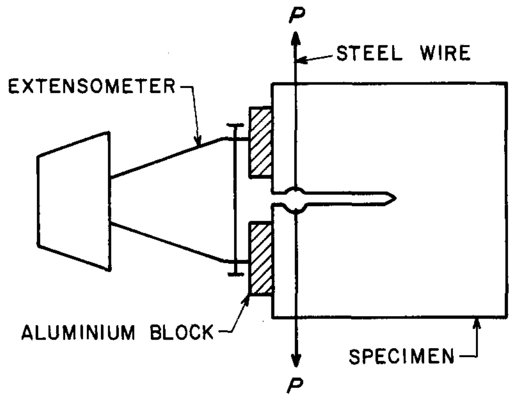

*Figure 4* Experimental arrangement for fracture tests.

in a similar manner to determine the flexural strengths and the static elastic moduli. Young's modulus, $E'$, was calculated from the slope of the linear portion of the load against time curves corrected for the machine and test fixture compliances; and the flexural strength, $\sigma_f$, from the load at failure. Specimen dimensions (mm) were: $W = B = 4$, $L = 50$ for $D_{ab}$; $W = 1.5$, $B = 4$, $L = 50$ for $D_{bc}$; and $W = 3.5$, $B = 10$, $L = 42$ for $D_{ca}$. The span $S$ was 38.1 mm in all cases. Very thin specimens ($W/S = 0.04$) were required for the $D_{bc}$ orientation to avoid basal plane shear delamination near the neutral axis. Four thicknesses of the pyrolytic carbon were glued together with cianoacrylate adhesive to make the $D_{ca}$ specimens since the 11 mm plate thickness was insufficient.

## 5. Results and discussion

### 5.1. Flexural strengths and elastic moduli

The flexural strengths, $\sigma_f$, and elastic moduli, $E'$ ($= E/(1 - \nu^2)$ for plane strain and $= E$ for plane stress) were measured for several specimens in each of the three deformation orientations and their averages are listed in Table I. Values reported for a similar pyrolytic carbon by Pappis and Blum [6, 11] are also listed for comparison. Elastic moduli were calculated from the observed compliances $C$ using the relationship [10]:

$E' = (1/BC)\ (S/W)^2[S/(4W) + (1 + \nu)/(2S/W)]$. The contribution of the term containing $\nu$ is very small when $(S/W) > 10$, the case here. Although this term was dropped in [11], it was retained here, setting $\nu = 0$ since the variation in $E'$ is $< 3\%$ for $0 \leqslant \nu \leqslant 1$.

The strengths for $D_{ab}$ and $D_{bc}$ layer rupture are comparable in magnitude, but 15 to 20 times larger than the $D_{ca}$ delamination strength. The $D_{ab}$ and $D_{bc}$ elastic moduli are also four to five times that for $D_{ca}$. These differences are consistent with the different nature of the bonding within the layers (covalent) and between the layers (van der Waal's). The modulus ratio is smaller than that for single crystal graphite because of the layer misorientation in the pyrolytic carbon, and perhaps a higher interlayer shear stiffness in the disordered pyrolytic carbon structure.

The layer rupture strengths and elastic moduli reported in Table I agree with those of Pappis and Blum [11], but their delamination strength and modulus are about twice the present values. This can probably be associated with differences in both the preferred orientation textures and the material densities. The RMS layer misorientation angle of only 17.5° for the present material is somewhat lower than values typically reported for pyrolytic carbons deposited at 2100 to 2200° C, about 20.5° for substrate-nucleated and even higher values for continuously nucleated structures [12]. Moreover, the 2.20 g cm$^{-3}$ density [11] is closer to the ideal turbostratic value of $\geqslant 2.21$ g cm$^{-3}$ (dependent on the $d_{002}$ value).

### 5.2. Fracture surfaces

Fractographic observations on the fracture mechanics specimens suggest that the toughness is quite anisotropic, increasing in the order $S_{ca}$, $S_{ab}$, $S_{cb}$. Scanning electron micrographs (SEM) of the fracture surfaces are shown in Fig. 5. Figs. 5a, b and c were taken at a low acceleration voltage (5 kV) and a zero tilt angle. Fig. 5d shows the same area as Fig. 5c, but tilted 45° (and at 20 kV) to illustrate more clearly the characteristic roughness of the $S_{bc}$ surfaces; a portion of the deposition surface on the compression side of the sample is also visible at the bottom of this micrograph.

These fracture surface micrographs agree very well with previous observations that the three fracture orientations exhibit entirely different features [7, 8]. Except for some cleavage steps and fracture debris, the

TABLE I Elastic moduli, strengths, and toughnesses of pyrolytic carbon. The values in parentheses are from [6, 11]

(a) MOR specimens (un-notched)

| Property | Orientation | | |
|---|---|---|---|
| | $D_{ab}$ | $D_{bc}$ | $D_{ca}$ |
| $E'$(GPa) | 28.1 ± 0.5 | 20.1 ± 0.5 | 5.5 ± 0.5 |
| | (26.2) | (23.1) | (10.7) |
| $\sigma_f$(MPa) | 190 ± 1 | 158 ± 7 | 9.6 ± 2 |
| | (183) | (165) | (20.7) |

(b) Fracture mechanics specimens (notched)

| Property | Orientation | | | |
|---|---|---|---|---|
| | $S_{ab}$ (CT) | $S_{bc}$ (CT) | $S_{bc}$ (three-point) | $S_{ca}$ (DCB) |
| $E^*$ (GPa) | 27 ± 2 | 12 ± 2 | – | 13 ± 2 |
| $\mathcal{G}_{Ic}$(J m$^{-2}$) | 37.8 ± 10 | – | – | 22.2 ± 5 |
| $J_{Ic}$(J m$^{-2}$) | 34.4 ± 5 | – | – | 21.1 ± 4 |
| $K_{Ic}$(MPa m$^{1/2}$) | 0.93 ± 0.10 | – | 7.5 to 1.4 | 0.53 ± 0.05 |

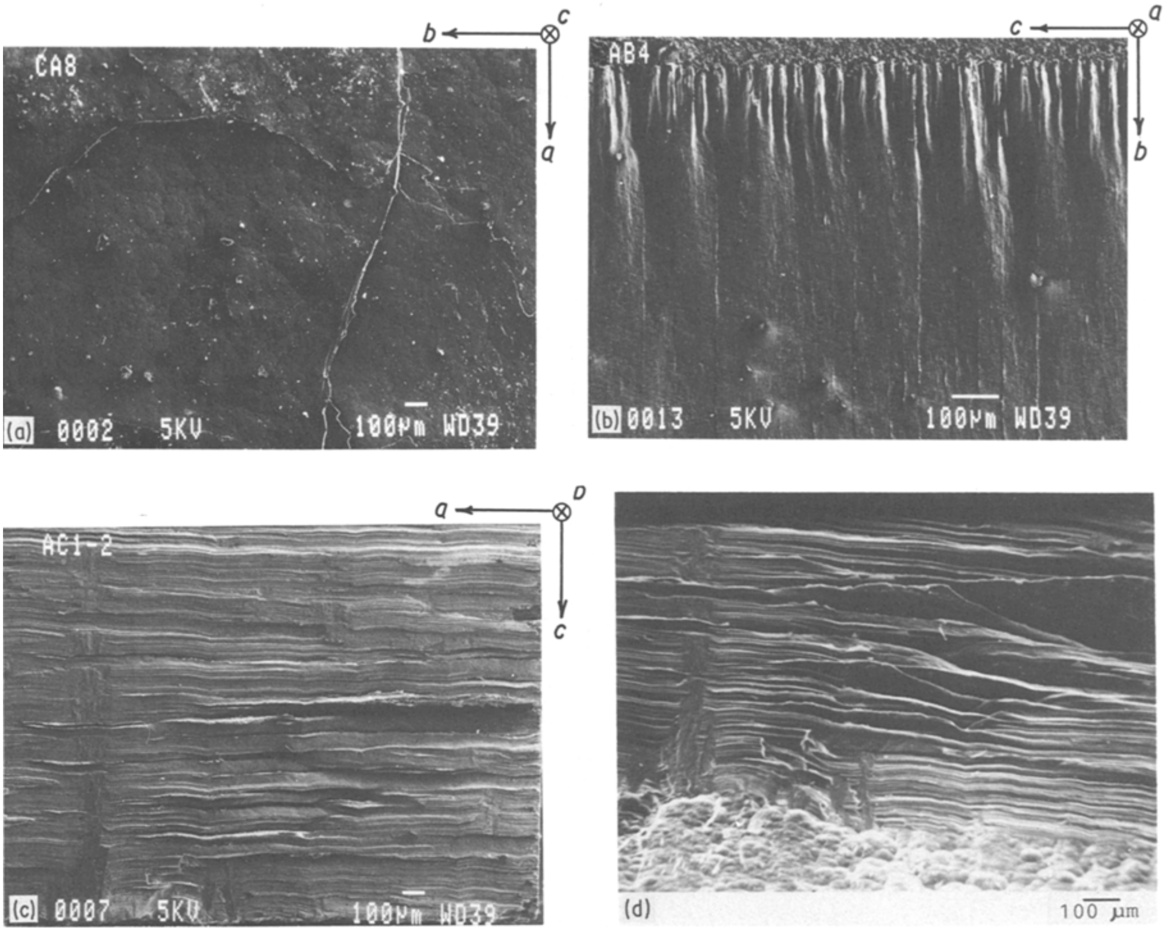

*Figure 5* Scanning electron micrographs of fracture surfaces: (a) $S_{ca}$ (DCB), (b) $S_{ab}$ (CT), (c) $S_{bc}$ (three-point bend), all zero tilt; (d) $S_{bc,}$ same area at 45° tilt.

$S_{ca}$ delamination fracture surface shown in Fig. 5a virtually replicates the as-deposited surface. The nodular "growth cone" morphology characteristic of pyrolytic carbon can be seen here and also at the bottom of Fig. 5d (where it is accented by the high viewing angle). Although the $S_{ab}$ and $S_{bc}$ layer rupture orientations differ only in the direction of crack propagation, the resulting fracture surfaces are quite different from each other, as well as from the $S_{ca}$ surfaces. The $S_{ab}$ surface, Fig. 5b, is fairly smooth at distances $\geqslant 100\,\mu$m from the notch tip (visible at the top of the micrograph). However, some small steps, evident as bright lines on the micrograph, persist parallel to the crack propagation direction. These result from basal cleavage joining segments of the main crack propagating along slightly different $S_{ab}$ paths, and thus comprise a hackle-type of feature that follows the local layer orientation. The "waviness' of these features reveals the wrinkled sheet structure characteristic of pyrolytic carbon. At much higher magnifications, the areas that appear smooth here are seen to be slightly rougher, on a $\leqslant 1\,\mu$m scale, perhaps corresponding to a fine substructure [8].

The $S_{bc}$ fracture surface, shown in Figs. 5c and d, appears very rough even at low magnifications, and comprises layer plane packets ruptured alternately above and below the average fracture plane. The wrinkled sheet structure is evident on these surfaces and traces of primary and sub-cone boundaries of the columnar structure can be identified. The $S_{bc}$ surface evidently results from crack propagation alternately across and between the layers, and is a consequence of the intensely anisotropic structure. Indeed, macroscopic crack branching due to delamination was commonly observed and had an important effect on the apparent toughness for $S_{bc}$ fracture as discussed in Sections 5.4 and 5.5. An example is shown in Fig. 6. The lengths and numbers of these delaminations differed substantially from specimen to specimen. Detailed examination using a fluorescent liquid penetrant revealed that delamination microcracks were present even in those specimens where macroscopic

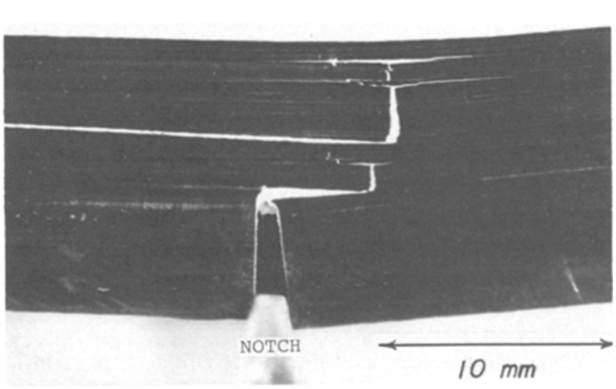

*Figure 6* Macroscopic crack branching due to delamination in an $S_{bc}$-oriented bend specimen ($W$ = 11 mm).

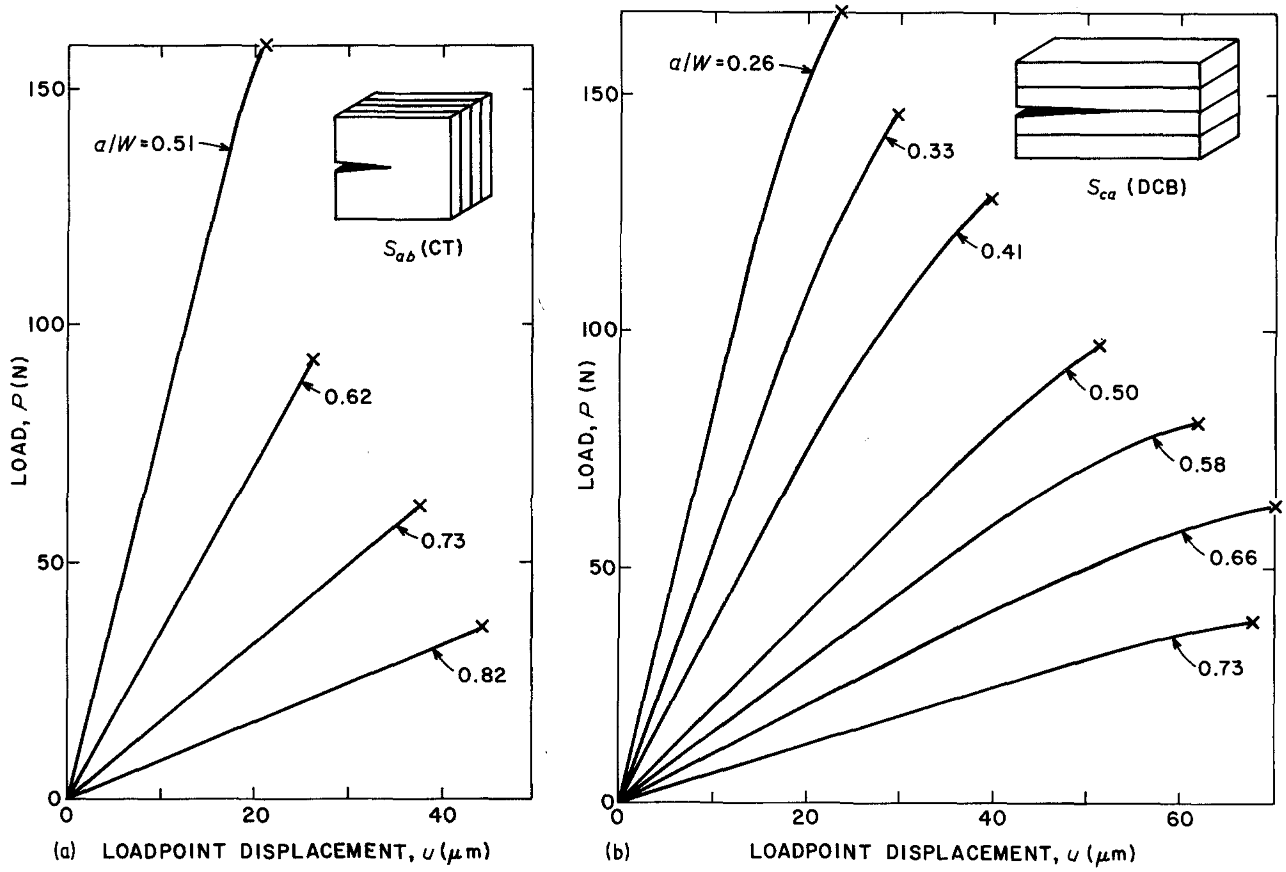

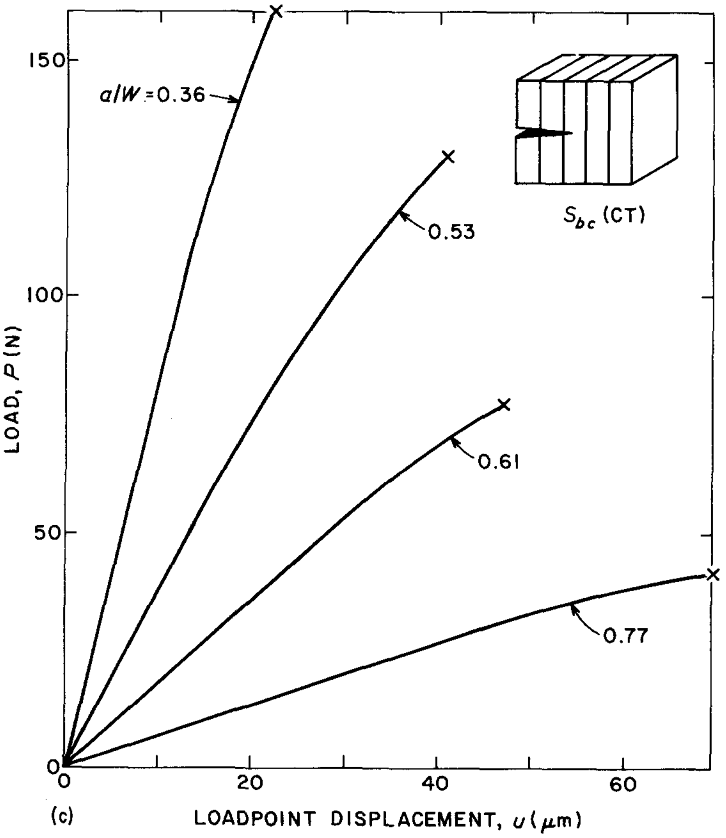

*Figure 7* Load against loadpoint displacement curves for (a) $S_{ab}$, (b) $S_{ca}$ and (c) $S_{bc}$-oriented specimens with different notch depths $a/W$.

delamination was not obvious. This is consistent with the SEM observations.

These fractographic indications of toughness anisotropy are confirmed by the fracture mechanics measurements, as shown by the values in Table I and described in the following sections.

### 5.3. Fracture toughnesses of $S_{ca}$ and $S_{ab}$ orientations

The load against loadpoint displacement ($P$–$u$) curves of the DCB and CT specimens for various notch lengths are shown in Fig. 7 for the three orientations. Linear behaviour was observed only for the $S_{ab}$ specimens,

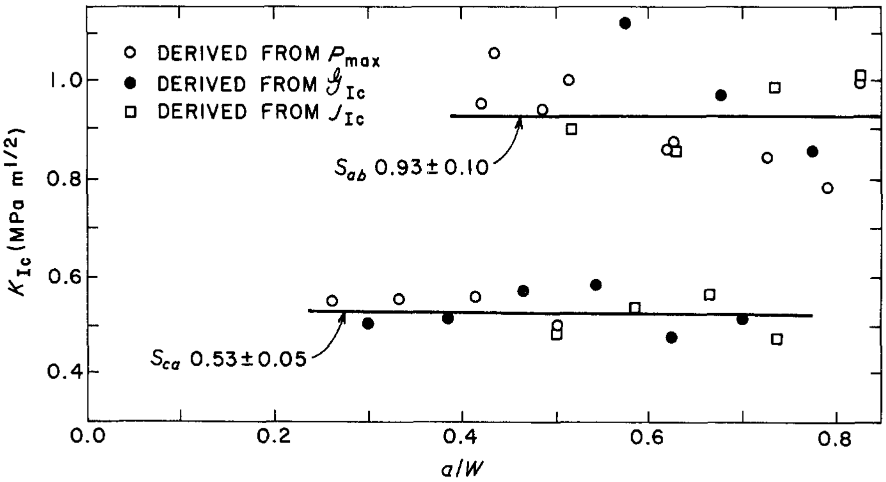

*Figure 8* Fracture toughness values $K_{Ic}$ derived from the maximum load $P_{max}$ and the energy parameters $\mathcal{G}_{Ic}$ and $J_{Ic}$ for $S_{ab}$ and $S_{ca}$ orientation fractures with various $a/W$.

Fig. 7a. The non-linear curves for the $S_{ca}$ and $S_{bc}$ orientations (Figs. 7b and c) may result from the slow growth of subcritical delamination cracks during loading. Although no direct evidence was obtained for this process, both of these specimen orientations ultimately failed by delamination. Small features consistent with delamination events were often seen in the $S_{bc}$ load/displacement data prior to failure. The $S_{bc}$ fracture toughnesses could not be determined from the Fig. 7c data because of the premature cleavage failure of these specimens.

For the $S_{ab}$ and $S_{ca}$ orientations, fracture toughnesses were determined three different ways. The critical stress intensity factor, $K_{Ic}$, was calculated directly from $P_{max}$ using the relation

$$K_{Ic} = YP_{max}/(BW^{1/2}) \qquad (1)$$

where the dimensionless factor, $Y$, depends on the specimen geometry and dimensions [10, 13, 14]. For the $S_{ca}$-oriented DCB specimens,

$$Y = (12)^{1/2}(W/H)^{1/2}[(a/H) + 0.7] \qquad (2a)$$

which is valid for $\alpha = (a/W) \leqslant [1 - (2H/W)] = 0.5$ for these specimens. For the $S_{ab}$-oriented CT specimens,

$$Y = \alpha F/(1 - \alpha)^{3/2} \qquad (2b)$$

where the detailed form of $F$ is discussed by Munz *et al.* [14]. The specimen dimensions $a$, $B$, $W$ and $H$ are those given in Fig. 3. The $K_{Ic}$ values determined in this manner are represented by the open circles in Fig. 8.

The fracture energy parameters $\mathcal{G}_{Ic}$ and $J_{Ic}$ were also determined from the load displacement data, and $K_{Ic}$ values were derived from them using the Irwin relations [13],

$$K_{Ic} = (\mathcal{G}_{Ic}E^*)^{1/2} = (J_{Ic}E^*)^{1/2} \qquad (3)$$

where $E^*$ is the effective elastic modulus of the appropriate fracture mechanics specimens. For anisotropic materials, $E^*$ generally differs from the conventional Young's modulus, $E'$, because the elastic strain in the notched $S_{ij}$ specimens results from a combination of two different types of deformation, $D_{ij}$ and $D_{ji}$, each with different elastic moduli. In the specimens for $S_{ca}$ fracture, the deformation is a mixture of $D_{bc}$ in the beam and $D_{ca}$ in the ligament. An analogous situation occurs for the $S_{bc}$ CT specimens. However, for the $S_{ab}$ specimens only a single type of deformation is involved because the $a$ and $b$ directions are equivalent. Consequently, $E^* = E'$ for this orientation.

Appropriate $E^*$ values may be estimated from the observed initial compliances $C(\alpha)$ determined from the load–displacement curves using the relationship [14, 15],

$$E^* = 2[C(\alpha)BW]^{-1} \int_0^a Y^2(a/W)\, \mathrm{d}a \qquad (4)$$

where the correction term involving the compliance of an unnotched specimen has been deleted because it is negligible for these samples. The integration may be done analytically for the DCB geometry so that $E^*$ can be computed directly. For the CT geometry, where numerical intergration is required, the value was determined as that which yields the best fit of the computed compliances to the observed values. The $E^*$ values for the three fracture specimen orientations are listed in Table I. The agreement between $E^*$ and $E'$ for the $S_{ab}$ orientation confirms the validity of the estimation procedure. The $E^*$ values for the $S_{ca}$ and $S_{bc}$ orientations are intermediate between the $E'$ values for these orientations as expected, and also of a comparable magnitude.

The critical energy release rate for crack extension is defined by $\mathcal{G}_{Ic} = \Delta U/(B\Delta a)$ where $\Delta U$ is the area between adjacent ($P$–$u$) curves corresponding to initial crack lengths $a$ and $a + \Delta a$, and $B$ is the specimen thickness. The $J$-integral was estimated using Rice's approximation [13], $J_{Ic} = 2A/[B(w - a)]$ where $A$ is the area under the ($P$–$u$) curve. This approximation is valid only for short ligaments and used only for $\alpha \geqslant 0.5$. The average values obtained for these two energy toughness parameters are given in Table I. The fracture toughness values derived from individual energy measurements using Equation 3 are shown in Fig. 8 by the filled circles and open squares and agree well with those determined from $P_{max}$. This agreement indicates that the linear elastic assumption for the plane strain fracture toughness is valid for both $S_{ab}$ and $S_{ca}$ fractures of this pyrolytic carbon over the range of crack-lengths investigated, despite the non-linearity of the $S_{ca}$ orientation ($P$–$u$) curves.

The average fracture toughness values, corresponding to the solid lines in Fig. 8, are 0.53 MPa m$^{1/2}$ for $S_{ca}$ fracture and 0.93 MPa m$^{1/2}$ for $S_{ab}$ fracture. This $S_{ab}$ toughness is comparable to published values for polygrannular synthetic graphites [2–5]. The low $S_{ca}$

toughness, only about half of the $S_{ab}$ value, further illustrates the anisotropy effects of the weak van der Waal's interlaminar bonding. According to a simple atomistic model for crack initiation, $K_{\mathrm{Ic}}$ is proportional to $E'\lambda^{1/2}$, where $\lambda$ is the interatomic distance [13]. The measured values of $E'$ for the $D_{ab}$ and $D_{ca}$ orientations listed in Table I and the $\lambda$ values for the $a$- and $c$- directions of pyrolytic carbon ($\sim 0.142$ and 0.344 nm, respectively) yield a calculated ratio of $K_{\mathrm{Ic}}(S_{ab})/K_{\mathrm{Ic}}(S_{ca}) \sim 3$ which is comparable to the experimental ratio of $\sim 2$. However, the observed ratio of the flexural strengths for these two orientations is considerably larger. Applying the relation $\sigma_{\mathrm{f}} c^{*1/2} \propto K_{\mathrm{Ic}}$, where $c^*$ is the critical flaw size dominating the flexural strength, it becomes evident that the low $D_{ca}$ flexural strength must result in large part from the presence of large interlaminar flaws. It is reasonable to expect that some of the $\sim 1\%$ microporosity in this pyrolytic carbon occurs in the form of interlaminar defects. Additional delamination microcracks may also have been generated during specimen preparation.

### 5.4. Toughness of the $S_{bc}$ orientation

Some of the most interesting observations during the present investigation are the high apparent experimental toughnesses observed for the $S_{bc}$ orientation fracture, shown by the open symbols in Fig. 9. These values were calculated from the observed $P_{\max}$ data for three-point bend specimens, using Equation 1 with

$$Y = 1.5\,(S/W)\,\Gamma_{\mathrm{M}}\alpha^{1/2}/(1-\alpha)^{3/2} \qquad (5)$$

where

$$\Gamma_{\mathrm{M}} = 1.99 - 1.33\alpha - (3.49 - 0.68\alpha + 1.35\alpha^2) \times (1-\alpha)(\alpha)/(1+\alpha)^2$$

after [10]. These apparent toughness values are 4 to 8 times as large as those observed for the $S_{ab}$ orientation layer rupture fractures. Although there is considerable scatter in these results, the maximum value obtained, 7.5 MPa m$^{1/2}$, is comparable to some of the toughest brittle ceramic materials at room temperature [16].

Extensive, macroscopic crack branching in the form of delaminations occurred in several of the $S_{bc}$-oriented specimens as illustrated in Fig. 6. These delaminations were directly associated with multiple crack arrests during the main-crack propagation as illustrated by the ($P$–$u$) curves in Fig. 10. The compliance increase as the load approaches a $P_{\max}$ is typical for the $S_{bc}$-oriented specimens and can probably be attributed to the nucleation or development of delaminations prior to the initiation of macrofracture processes. The arrows indicate probable points of the onset of delamination processes which were usually signaled explicitly by a minute load drop, and sometimes by an audible acoustic emission. The extent of the compliance increase as well as the number, size and distribution of delamination cracks which could be observed after failure varied considerably from specimen to specimen. However, the fracture surfaces of all of the $S_{bc}$ orientation specimens that yielded $K_{\mathrm{Ic}}^{\mathrm{app}} \geqslant 5$ MPa m$^{1/2}$ were characterized by an obvious delamination at, or very near to the tip of the original notch. In one instance, that of the specimen with $\alpha = 0.59$, all of the delaminations appeared to occur in the ligament ahead of the notch tip. It is noteworthy that the apparent toughness of that particular specimen was also smaller, only about 3.8 MPa m$^{1/2}$.

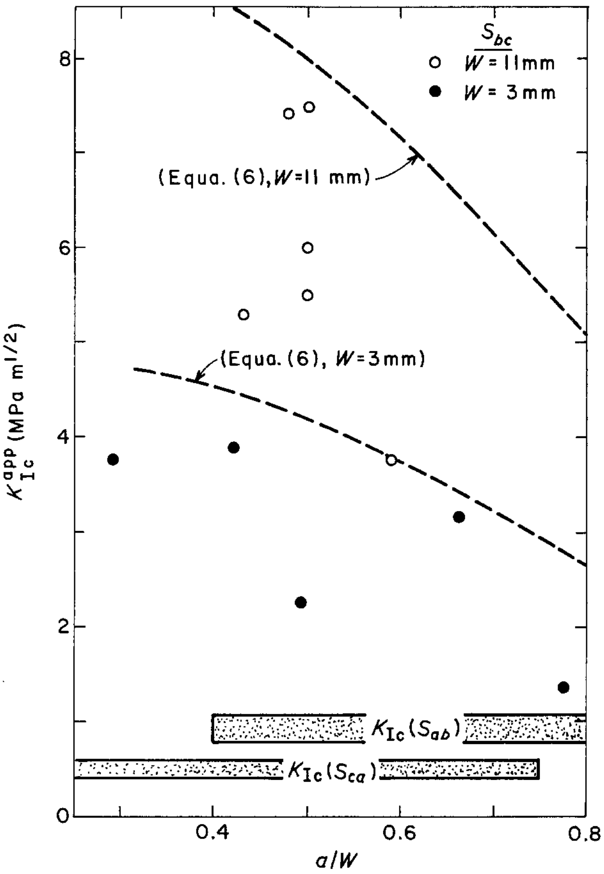

*Figure 9* Apparent fracture toughnesses of $S_{bc}$-oriented bend specimens, determined from $P_{\max}$ for two thicknesses $W$ and various notch depths. Broken lines show calculated delamination-toughening maxima.

These results indicate that a process of "induced delamination toughening" is responsible for the high apparent toughness values observed for the $S_{bc}$-oriented specimens. Delamination microcracking at the main crack tip is not a new toughening process, having been discussed by Cook and Gordon [17] two decades ago. In the present case, it may be related in part to the shear stress developed during the bend test. Delamination ahead of the main crack tip can contribute to increased fracture resistance in at least two ways [13, 17]. One factor is the obvious reduction of the normal stress, $\sigma_{xx}$ in the direction of the crack extension as a consequence of the generation of the internal delamination free-surfaces. This results in a decrease of the stress intensity factor, $K_{\mathrm{I}}$ at the main crack tip. More importantly, delamination ahead of the main crack reduces the crack tip acuity when the main crack actually encounters the delamination surface. The crack blunting process has a very strong effect of decreasing the $K_{\mathrm{I}}$ value at the crack tip and can completely dominate the crack propagation process. The crack arrests observed experimentally in Fig. 10 are a direct result of this crack blunting process, as are the high apparent toughness values obtained from $P_{\max}$ when delamination actually occurs at the main-crack tip.

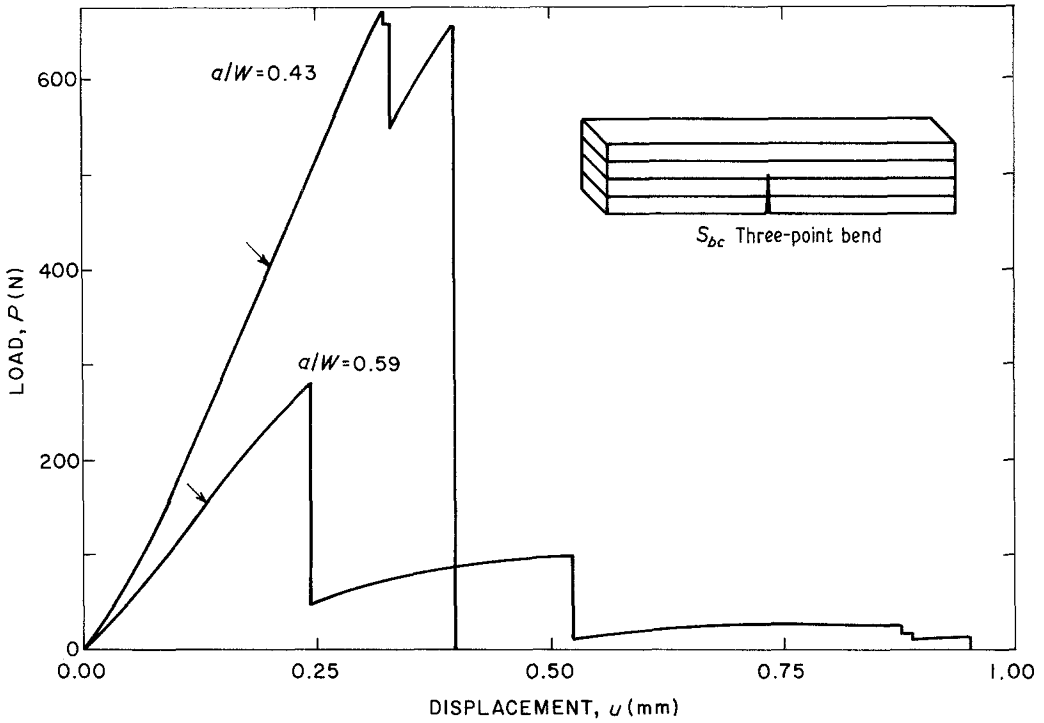

*Figure 10* Load against displacement curves for $S_{bc}$-oriented bend specimens with $W = 11$ mm and two notch depths. Arrows mark initial delamination events.

The rapid decrease in the apparent toughness with increasing $\alpha$ for the $S_{bc}$ orientation fractures as indicated by the open data points in Fig. 9 suggests that the intrinsic $S_{bc}$ fracture toughness, in the absence of any macroscopic delamination cracking, is probably less than 3 MPa m$^{1/2}$. However, the large scatter and the limited $\alpha$ range of these results does not permit a confident estimate of the intrinsic value. To obtain additional information about the $S_{bc}$ orientation fracture, additional tests were completed using bend specimens with a smaller cross-sectional area ($W = B = 3$ mm) and for a wider range of $\alpha$ values under the premise that the tendency for delamination might be reduced by a smaller ligament length, and therefore allow a direct experimental determination of the intrinsic toughness. The apparent toughness values obtained with these smaller specimens, shown by the solid symbols in Fig. 9, are indeed much lower, but the data scatter is still present and the values still decrease as $\alpha$ increases. Furthermore, these specimens failed in exactly the same manner as the larger ones, with delamination at the notch tip preceding the initiation of layer rupture. Crack branching and multiple crack arrests also occurred during failure. It must be concluded that the delamination process is characteristic of $S_{bc}$ orientation failures over a wide range of $W$ and $\alpha$ values. This delamination can be attributed directly to the combined influences of the strong structural anisotropy of the pyrolytic carbon and the shear and perpendicular-to-layer components of the stress distribution at the main crack tip. The scatter of apparent toughness values which was observed for the $S_{bc}$ orientation failures can probably be attributed to the sample-to-sample variation of the size and distribution of these delaminations, coupled with the strong influences of the delamination process. These variations may in turn result from differences in the local internal stresses, the influence of microstructural variations in the vicinity of the advancing crack tip, and also from possible damage associated with the specimen preparation.

The general trends of the observed apparent toughness values with $W$ and $\alpha$ can be appreciated from a simple extreme-case model: if a delamination occurs exactly at the notch tip and is sufficiently long, the fracture load, $P_{\max}$, can be approximated by the bending-failure load, $P_f$, of an unnotched specimen of thickness $(W - a) = W(1 - \alpha)$, i.e. the remaining ligament of the notched specimen. Then, $P_{\max} \approx P_f = 2BW^2(1 - \alpha)^2\sigma_f/(3S)$, and using Equations 1 and 5,

$$K_{Ic}^{app}(\max) \approx \sigma_f W^{1/2}(1 - \alpha)^{1/2}\alpha^{1/2}\Gamma_M \qquad (6)$$

Thus, $K_{Ic}^{app}(\max)$, the maximum apparent fracture toughness calculated from the observed $P_{\max}$ when the stress concentration at the notch tip is reduced to zero by the delamination mechanism, is predicted to be proportional to the square root of the specimen dimension $W$, and to vary with the notch depth as $[\alpha(1 - \alpha)]^{1/2}\Gamma_M$. The values predicted by Equation 6 for the two $W$ values used here and the measured $D_{bc}$ flexural strength in Table I are shown by the two broken curves in Fig. 9. It is noteworthy that the highest experimentally observed toughness values approach the calculated limits for each case; and that the trends of the dependence on both $W$ and $\alpha$ are consistent with Equation 6. This provides further support for the proposed induced delamination toughening mechanism.

The intrinsic toughness for fracture in the $S_{bc}$ orientation may be estimated by considering the minimum experimental values in Fig. 9. On that basis, it is $\leqslant 1.4$ MPa m$^{1/2}$ and therefore comparable to the value for $S_{ab}$ fracture. Physically, the intrinsic toughnesses for these two orientations should be similar because both comprise rupture of the covalent intralayer bonds, a point which is further substantiated by the similarity of their measured flexural strengths. The greater roughness of the $S_{bc}$ fracture surface results mainly from the occurrence of small segments of low-energy cleavage surface or delamination cracks. The presence of these could account for a slightly greater $S_{bc}$ toughness.

### 5.5. Delamination toughening

Cook and Gordon [17] appear to have been the first to recognize the importance of delamination microcracking as a toughening mechanism, noting that secondary failures at weak interfaces oriented perpendicular to the main crack could result in increases of the strength and also in the fracture toughness of a brittle material. Kelly [18] subsequently discussed this type of toughening mechanism with respect to the failure of unidirectional fibrous composites. Delamination microcrack toughening can be considered with that of toughening by a general process zone of microcracks surrounding the main crack tip as discussed initially by Hoagland *et al.* [19] and more recently by Evans and Faber [20], among others.

A general description of delamination toughening may be developed by considering a material in which delamination cracks are induced during extension of the main crack. The actual stress intensity factor $(K_\mathrm{I})_\mathrm{del}$ at the crack tip experiencing stress reduction due to delamination microcracking may be written as

$$(K_\mathrm{I})_\mathrm{del} = Y_\mathrm{del} P/(BW^{1/2}) \qquad (7)$$

where $Y_\mathrm{del}$ is the dimensionless geometric factor of the main crack tip adjacent to delamination cracks. $Y_\mathrm{del}$ will always be smaller than the $Y$ values defined by Equations 2 or 5. The apparent stress intensity factor, $K_\mathrm{I}^\mathrm{app} = YP/(BW^{1/2})$, can then be written in terms of the actual stress intensity factor as

$$K_\mathrm{I}^\mathrm{app} = (Y/Y_\mathrm{del})(K_\mathrm{I})_\mathrm{del} \qquad (8)$$

where the toughening factor $(Y/Y_\mathrm{del})$ is always greater than unity because of the reduction in stress level due to the delamination crack array. It is a function of the size, number and distribution of the delamination cracks, which may be influenced by the main-crack length, the specimen geometry and the test method as well as by material characteristics that affect the microcracking propensity of the material. $Y$ values for various crack arrays have been summarized by Sih [21], but the specific situation of a delamination crack that is perpendicular to the main crack has not been solved.

It is also possible that the fracture toughness could be decreased by the presence of microcracks for they may join the main crack and thus enhance crack extension. In that situation,

$$K_\mathrm{Ic} = f(\varrho_\mathrm{c})K_\mathrm{Ic}^\mathrm{i} \qquad (9)$$

where $\varrho_\mathrm{c}$ is the delamination crack density and $K_\mathrm{Ic}^\mathrm{i}$ is the intrinsic fracture toughness of the material without delamination microcracks. The embrittling factor, $f(\varrho_\mathrm{c})$, will be less than unity. At the critical condition for the onset of unstable crack propagation, $(K_\mathrm{I})_\mathrm{del} = K_\mathrm{Ic}$, and Equations 8 and 9 may be combined to give

$$K_\mathrm{Ic}^\mathrm{app} = (Y/Y_\mathrm{del})f(\varrho_\mathrm{c})K_\mathrm{Ic}^\mathrm{i} = DK_\mathrm{Ic}^\mathrm{i} \qquad (10)$$

The magnitude of the combined coefficient, $D = (Y/Y_\mathrm{del})f(\varrho_\mathrm{c})$, is determined by the relative magnitudes of the toughening and the embrittling factors, which will depend on the delamination crack distribution. Thus, the apparent fracture toughness, $K_\mathrm{Ic}^\mathrm{app}$, is a variable which depends on the main crack length, the specimen geometry, etc., as well as the intrinsic toughness of the material. Experimental evaluation of either $D$ or $K_\mathrm{Ic}^\mathrm{i}$ may be quite difficult. However, the results obtained here suggest that $D$ can exceed five for the notched three-point bend measurements of pyrolytic carbon. Furthermore, for this geometry, the maximum $K_\mathrm{Ic}^\mathrm{app}$ values obtainable from delamination toughening can be estimated from directly measured parameters using Equation 6. As is evident from Fig. 9, the calculated values are consistent with the observed results for a range of specimen dimensions and initial crack lengths.

## 6. Conclusions

The anistropic fracture characteristics of an as-deposited pyrolytic carbon were investigated by measuring the fracture thoughnesses, flexural strengths and elastic moduli for three orientations. Nomenclature was introduced for designating the three distinct flexural deformations and corresponding crack-opening fracture surface orientations in this and other laminar materials. The toughnesses were determined by linear fracture mechanics and energy methods over a wide range of initial crack lengths, and the fracture surfaces were examined by scanning electron microscopy.

For basal cleavage ($S_{ca}$ fracture) and layer rupture parallel to the layers ($S_{ab}$) the fracture surfaces are smooth; $K_\mathrm{Ic}$ is independent of crack length; and the toughness values computed from the maximum load at fracture agree with those derived from the measured energy parameters $\mathcal{G}_\mathrm{Ic}$ and $J_\mathrm{Ic}$, validating the linear elasticity assumption. The $S_{ca}$ toughness is quite low, $K_\mathrm{Ic} \simeq 0.5\,\mathrm{MPa\,m^{1/2}}$, while that for layer rupture is nearly twice as large. Greater anisotropies were found for the strengths and Young's moduli. These results are consistent with the bonding anisotropy and the microstructure.

Although the intrinsic toughness for layer rupture by $S_{bc}$ crack propagation across the layers appears to be comparable to that for $S_{ab}$ rupture along the layers, the experimental results for these two orientations are quite different. Rough fracture surfaces, crack arrests during failure, and large apparent toughness values (as much as an order of magnitude higher than for $S_{ab}$ fracture) that depend strongly on specimen size and crack length were observed for $S_{bc}$ fracture. All of these phenomena result directly from delamination microcracking that accompanies the failure. Delamination is a consequence of the large structural anisotropy of pyrolytic carbon, and is favoured by the shear stresses that accompany loading of the $S_{bc}$-oriented specimens. The general characteristics of this induced delamination toughening process were described phenomenologically and the upper limit of the apparent toughness was defined as a function of specimen size and initial crack length by a simple model for the notched bend geometry used in the present measurements.

## Acknowledgements

One of the authors (M.S.) was partially supported by the Japanese Ministry of Education. The assistance of Y. Hishiyama, Musashi Institute of Technology and M. Inagaki of Toyohashi University of Technology, Japan with the SEM fractography is appreciated.

## References

1. B. T. KELLY, "Physics of Graphite" (Applied Science, London, 1981) Ch. 3.
2. J. L. WOOD, R. C. BRADT and P. L. WALKER Jr, *Carbon* **18** (1980) 179.
3. J. L. WOOD, J. X. ZHAO, R. C. BRADT and P. L. WALKER Jr, *ibid.* **19** (1981) 61.
4. J. X. ZHAO, J. L. WOOD, R. C. BRADT and P. L. WALKER Jr, *ibid.* **19** (1981) 405.
5. M. SAKAI, K. URASHIMA and M. INAGAKI, *J. Amer. Ceram. Soc.* **66** (1983) 868.
6. W. H. SMITH and D. H. LEEDS, in "Modern Materials", Vol. 7 (Academic Press, New York, 1970) pp. 165–80.
7. J. M. BERRY and J. J. GEBHARDT, *J. Amer. Ceram. Soc.* **48** (1965) 350.
8. D. B. FISCHBACH and D. R. UPTEGROVE, Semi-annual Progress Report no. 2, NASA grant, NGR-48-002-129, "Structural Studies on Carbon Materials for Aerospace Refractory Applications", 27 December (1972).
9. D. B. FISCHBACH, *J. App. Phys.* **37** (1966) 2202.
10. D. MUNZ, R. T. BUBSEY and J. L. SHANNON Jr, *J. Amer. Ceram. Soc.* **63** (1980) 300.
11. J. PAPPIS and S. L. BLUM, *ibid.* **44** (1961) 592.
12. D. B. FISCHBACH, in "Chemistry and Physics of Carbon", Vol. 7, edited by P. L. Walker (Marcel Dekker, New York, 1971), pp. 1–105.
13. R. W. HERTZBERG, "Deformation and Fracture Mechanics of Engineering Materials" 2nd Edn. (Wiley, New York, 1983) Ch. 7 and 8.
14. D. MUNZ, R. T. BUBSEY, J. E. SRAWLEY, *Int. J. Fract.* **16** (1980) 359.
15. M. SAKAI and K. YAMASAKI, *J. Amer. Ceram. Soc.* **66** (1983) 371.
16. R. C. GARVIE, R. H. HANNINK and R. T. PASCOE, *Nature (London)* **258** (1975) 703.
17. J. COOK and J. E. GORDON, *Proc. R. Soc.* **A282** (1964) 508.
18. A. KELLY, *ibid.* **A319** (1970) 95.
19. R. G. HOAGLAND, G. T. HAHN and A. R. ROSENFIELD, *Rock Mech.* **5** (1973) 77.
20. A. G. EVANS and K. T. FABER, *J. Amer. Ceram. Soc.* **67** (1984) 255.
21. G. C. SIH, "Handbook of Stress Intensity Factors" (Institute of Fracture and Solid Mechanics, Lehigh University, Bethlehem, Pennsylvania, USA, 1973).

*Received 13 May*
*and accepted 12 June 1985*